

# An Adaptive Geometry-Based Stochastic Model for Non-Isotropic MIMO Mobile-to-Mobile Channels

Xiang Cheng, *Student Member, IEEE*, Cheng-Xiang Wang, *Senior Member, IEEE*,

David I. Laurenson, *Member, IEEE*, Sana Salous, *Member, IEEE*, and Athanasios V. Vasilakos, *Member, IEEE*

**Abstract**—In this paper, a generic and adaptive geometry-based stochastic model (GBSM) is proposed for non-isotropic multiple-input multiple-output (MIMO) mobile-to-mobile (M2M) Ricean fading channels. The proposed model employs a combined two-ring model and ellipse model, where the received signal is constructed as a sum of the line-of-sight, single-, and double-bounced rays with different energies. This makes the model sufficiently generic and adaptable to a variety of M2M scenarios (macro-, micro-, and pico-cells). More importantly, our model is the first GBSM that has the ability to study the impact of the vehicular traffic density on channel characteristics. From the proposed model, the space-time-frequency correlation function and the corresponding space-Doppler-frequency power spectral density (PSD) of any two sub-channels are derived for a non-isotropic scattering environment. Based on the detailed investigation of correlations and PSDs, some interesting observations and useful conclusions are obtained. These observations and conclusions can be considered as a guidance for setting important parameters of our model appropriately and building up more purposeful measurement campaigns in the future. Finally, close agreement is achieved between the theoretical results and measured data, demonstrating the utility of the proposed model.

**Index Terms**—Mobile-to-mobile channels, MIMO, non-isotropic scattering environments, space-time-frequency correlation function, space-Doppler-frequency power spectrum density.

## I. INTRODUCTION

RECENTLY, mobile-to-mobile (M2M) communications have received much attention due to some new applications, such as wireless mobile ad hoc networks [1], relay-based cellular networks [2], and dedicated short range communications (DSRC) for intelligent transportation systems

Manuscript received December 16, 2008; revised March 13, 2009 and May 12, 2009; accepted May 12, 2009. The associate editor coordinating the review of this paper and approving it for publication was K. K. Wong.

X. Cheng and C.-X. Wang are with the Joint Research Institute for Signal and Image Processing, School of Engineering and Physical Sciences, Heriot-Watt University, Edinburgh EH14 4AS, UK (e-mail: {xc48, cheng-xiang.wang}@hw.ac.uk).

D. I. Laurenson is with the Joint Research Institute for Signal and Image Processing, School of Engineering and Electronics, The University of Edinburgh, Edinburgh EH9 3JL, UK (e-mail: dave.laurenson@ed.ac.uk).

S. Salous is with the Center for Communication Systems, School of Engineering, University of Durham, Durham DH1 3LE, UK (e-mail: sana.salous@durham.ac.uk).

A. V. Vasilakos is with the Department of Computer and Telecommunications Engineering, University of Western Macedonia, GR 50100 Kozani, Greece (e-mail: vasilako@ath.forthnet.gr).

X. Cheng, C.-X. Wang, and D. I. Laurenson acknowledge the support from the Scottish Funding Council for the Joint Research Institute in Signal and Image Processing between the University of Edinburgh and Heriot-Watt University which is a part of the Edinburgh Research Partnership in Engineering and Mathematics (ERPem). This paper was presented in part at IEEE IWCMC'08, Crete, Greece, August 2008.

Digital Object Identifier 10.1109/TWC.2009.081560

(e.g., IEEE 802.11p standard) [3]. In contrast to conventional fixed-to-mobile (F2M) cellular radio systems, in M2M systems both the transmitter (Tx) and receiver (Rx) are in motion and equipped with low elevation antennas. For M2M communications, multiple-input multiple-output (MIMO) technology becomes more attractive since multiple antenna elements can be easily mounted on large vehicular surfaces. It is well-known that the design of a wireless system requires the detailed knowledge about the underlying propagation channel and a corresponding realistic channel model. Up to now, only few measurement campaigns had been conducted to investigate single-input single-output (SISO) M2M channels [4]–[8], even fewer to study MIMO M2M channels [9].

M2M channel models available in the literature can be categorized as deterministic models [10] and stochastic models, while the latter can be further classified as non-geometrical stochastic models (NGSMs) (also known as parametric models) [6] and geometry-based stochastic models (GBSMs) [11]–[14]. A deterministic M2M model based on the ray-tracing method was proposed in [10]. This model requires a detailed and time-consuming description of the propagation environment and consequently cannot be easily generalized to a wider class of scenarios.

A SISO NGSM proposed in [6] is the origin of the channel model standardized by IEEE 802.11p. This model determines physical parameters of a M2M channel in a completely stochastic manner by prescribing underlying probability distribution functions (PDFs) without presuming any underlying geometry. Therefore, this model offers no conceptual framework to facilitate meaningful generalization into different scenarios. In addition, this pure parameter-based model needs to jointly consider many parameters for modeling MIMO channels, which leads to high complexity [15].

A GBSM is derived from the predefined stochastic distributions of effective scatterers by applying the fundamental laws of wave propagation. Such a model can be easily adapted to different scenarios by changing the shape of the scattering region (e.g., one-ring, two-ring, or ellipse). More importantly, the application of the concept of effective scatterers significantly reduces the complexity of a GBSM since only single and/or double scattering effects need to be simulated [15]. Moreover, for modeling MIMO channels, a GBSM can avoid the inherent complexity problem of a NGSM as shown in [15]. In [11] and [12], the first GBSM was proposed for isotropic SISO M2M Rayleigh fading channels and corresponding statistical properties were investigated. In [13], a two-ring GBSM considering only double-bounced rays was presented for non-

isotropic MIMO M2M Rayleigh fading channels in macro-cell scenarios. In [14], the authors proposed a general two-ring GBSM with both single- and double-bounced rays for non-isotropic MIMO M2M Ricean channels in both macro- and micro-cell scenarios.

None of the above GBSMs is sufficiently general to characterize a wide variety of M2M scenarios, especially for pico-cell scenarios, which have recently been considered by some measurement campaigns [4]–[9]. As demonstrated in [8], the impact of the vehicular traffic density (VTD) on channel characteristics in micro- and pico-cell scenarios cannot be neglected, unlike in macro-cell scenarios. However, none of the existing GBSMs has the ability to take this impact into account. Although the Doppler power spectral density (PSD) is one of the most important statistics that significantly distinguish M2M channels from F2M channels, more detailed investigations of the Doppler PSD in non-isotropic scattering environments are surprisingly lacking in the open literature. Moreover, Doppler PSD characteristics for an ellipse M2M channel model are not yet known. Finally, frequency correlations of sub-channels with different carrier frequencies, studied in [16] for F2M channels, in M2M communications have not been studied so far, although orthogonal frequency-division multiplexing (OFDM) has already been suggested for use in IEEE 802.11p.

Motivated by the above gaps, in this paper we propose a new GBSM that addresses all the aforementioned shortcomings of the existing GBSMs. Based on the proposed model, the space-time-frequency (STF) correlation function (CF) and the corresponding space-Doppler-frequency (SDF) PSD are derived. The contributions and novelties of this paper are summarized as follows.

- 1) We propose a generic GBSM for narrowband non-isotropic MIMO M2M Ricean fading channels. The proposed model can be adapted to a wide variety of scenarios, e.g., macro-, micro-, and pico-cell scenarios, by adjusting model parameters.
- 2) By distinguishing between the moving cars and the stationary roadside environments in micro- and pico-cell scenarios, our model is the first GBSM to consider the impact of the VTD on M2M channel characteristics.
- 3) We propose a new general method to derive the exact relationship between the angle of arrival (AoA) and angle of departure (AoD) for any known shapes of the scattering region, e.g., one-ring, two-ring, or ellipse, in a wide variety of scenarios.
- 4) We point out that the widely used CF definition in [13], [14], [17], [18] is incorrect and is actually the complex conjugate of the correct CF definition as given in Stochastic Processes [19].
- 5) From the proposed model, we derive the STF CF and the corresponding SDF PSD, which are sufficiently general and can be reduced to many existing CFs and PSDs, respectively, e.g., those in [11], [13], [14], [17], [18]. In addition, our analysis shows that the space-Doppler PSD of a single-bounce two-ring model for non-isotropic MIMO M2M channels derived in [14] is incorrect.
- 6) Based on the derived STF CF and SDF PSD, we study in more detail the degenerate CFs and PSDs in terms

of some important parameters and thus obtain some interesting observations. Finally, the obtained theoretical Doppler PSDs and measurement data in [6] are compared. Excellent agreement between them demonstrates the utility of the proposed model.

The remainder of this paper is outlined as follows. Section II describes the new adaptive GBSM for narrowband MIMO M2M Ricean fading channels. In Section III, based on the proposed new model, the STF CF and the corresponding SDF PSD are derived. Numerical results and analysis are presented in Section IV. Finally, conclusions are drawn in Section V.

## II. A NEW ADAPTIVE GBSM FOR NON-ISOTROPIC MIMO M2M RICEAN FADING CHANNELS

Let us now consider a narrowband single-user MIMO M2M multicarrier communication system with  $M_T$  transmit and  $M_R$  receive omnidirectional antenna elements. Both the Tx and Rx are equipped with low elevation antennas. Fig. 1 illustrates the geometry of the proposed GBSM, which is the combination of a single- and double-bounce two-ring model, a single-bounce ellipse model, and the LoS component. As an example, uniform linear antenna arrays with  $M_T = M_R = 2$  were used here. The two-ring model defines two rings of effective scatterers, one around the Tx and the other around the Rx. Suppose there are  $N_1$  effective scatterers around the Tx lying on a ring of radius  $R_T$  and the  $n_1$ th ( $n_1 = 1, \dots, N_1$ ) effective scatterer is denoted by  $s^{(n_1)}$ . Similarly, assume there are  $N_2$  effective scatterers around the Rx lying on a ring of radius  $R_R$  and the  $n_2$ th ( $n_2 = 1, \dots, N_2$ ) effective scatterer is denoted by  $s^{(n_2)}$ . For the ellipse model,  $N_3$  effective scatterers lie on an ellipse with the Tx and Rx located at the foci. The semi-major axis of the ellipse and the  $n_3$ th ( $n_3 = 1, \dots, N_3$ ) effective scatterer are denoted by  $a$  and  $s^{(n_3)}$ , respectively. The distance between the Tx and Rx is  $D = 2f$  with  $f$  denoting the half length of the distance between the two focal points of the ellipse. The antenna element spacings at the Tx and Rx are designated by  $\delta_T$  and  $\delta_R$ , respectively. It is normally assumed that the radii  $R_T$  and  $R_R$ , and the difference between the semi-major axis  $a$  and the parameter  $f$ , are all much greater than the antenna element spacings  $\delta_T$  and  $\delta_R$ , i.e.,  $\min\{R_T, R_R, a - f\} \gg \max\{\delta_T, \delta_R\}$ . The multi-element antenna tilt angles are denoted by  $\beta_T$  and  $\beta_R$ . The Tx and Rx move with speeds  $v_T$  and  $v_R$  in directions determined by the angles of motion  $\gamma_T$  and  $\gamma_R$ , respectively. The AoA of the wave traveling from an effective scatterer  $s^{(n_i)}$  ( $i \in \{1, 2, 3\}$ ) toward the Rx is denoted by  $\phi_R^{(n_i)}$ . The AoD of the wave that impinges on the effective scatterer  $s^{(n_i)}$  is designated by  $\phi_T^{(n_i)}$ . Note that  $\phi_{R_q}^{LoS}$  denotes the AoA of a LoS path.

The MIMO fading channel can be described by a matrix  $\mathbf{H}(t) = [h_{pq}(t)]_{M_R \times M_T}$  of size  $M_R \times M_T$ . The received complex fading envelope between the  $p$ th ( $p = 1, \dots, M_T$ ) Tx and the  $q$ th ( $q = 1, \dots, M_R$ ) Rx at the carrier frequency  $f_c$  is a superposition of the LoS, single-, and double-bounced components, and can be expressed as

$$h_{pq}(t) = h_{pq}^{LoS}(t) + h_{pq}^{SB}(t) + h_{pq}^{DB}(t) \quad (1)$$

where

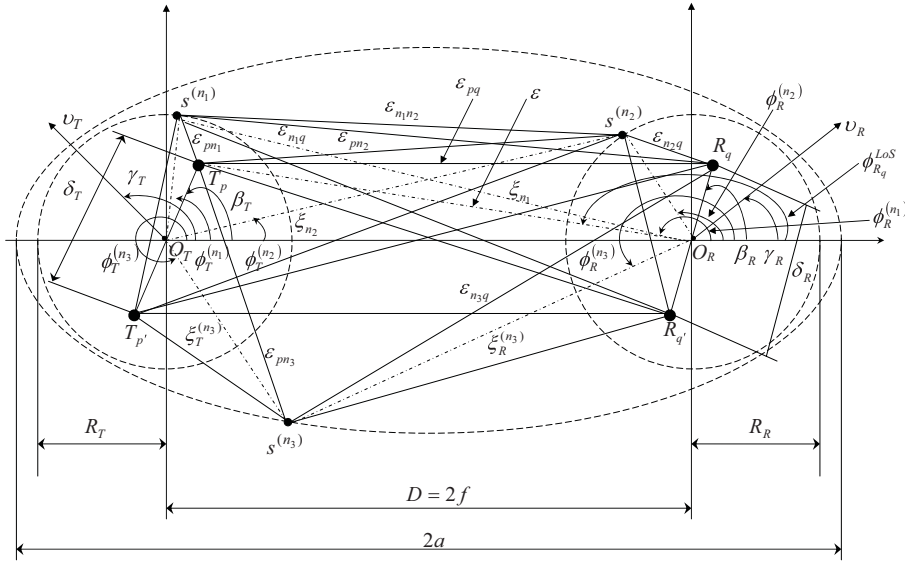


Fig. 1. A generic channel model combining a two-ring model and an ellipse model with LoS components, single- and double-bounced rays for a MIMO M2M channel ( $M_T = M_R = 2$ ).

$$h_{pq}^{LoS}(t) = \sqrt{\frac{K_{pq}\Omega_{pq}}{K_{pq} + 1}} e^{-j2\pi f_c \tau_{pq}} \times e^{j[2\pi f_{Tmax} t \cos(\pi - \phi_{R_q}^{LoS} + \gamma_T) + 2\pi f_{Rmax} t \cos(\phi_{R_q}^{LoS} - \gamma_R)]} \quad (2)$$

$$h_{pq}^{SB}(t) = \sum_{i=1}^I h_{pq}^{SB_i}(t) = \sum_{i=1}^I \sqrt{\frac{\eta_{SB_i}\Omega_{pq}}{K_{pq} + 1}} \lim_{N_i \rightarrow \infty} \sum_{n_i=1}^{N_i} \frac{1}{\sqrt{N_i}} e^{j(\psi_{n_i} - 2\pi f_c \tau_{pq, n_i})} \times e^{j[2\pi f_{Tmax} t \cos(\phi_T^{(n_i)} - \gamma_T) + 2\pi f_{Rmax} t \cos(\phi_R^{(n_i)} - \gamma_R)]} \quad (3)$$

$$h_{pq}^{DB}(t) = \sqrt{\frac{\eta_{DB}\Omega_{pq}}{K_{pq} + 1}} \lim_{N_1, N_2 \rightarrow \infty} \sum_{n_1, n_2=1}^{N_1, N_2} \frac{1}{\sqrt{N_1 N_2}} \times e^{j(\psi_{n_1, n_2} - 2\pi f_c \tau_{pq, n_1, n_2})} \times e^{j[2\pi f_{Tmax} t \cos(\phi_T^{(n_1)} - \gamma_T) + 2\pi f_{Rmax} t \cos(\phi_R^{(n_2)} - \gamma_R)]}. \quad (4)$$

In (2)–(4),  $\tau_{pq} = \varepsilon_{pq}/c$ ,  $\tau_{pq, n_i} = (\varepsilon_{pn_i} + \varepsilon_{n_i q})/c$ , and  $\tau_{pq, n_1, n_2} = (\varepsilon_{pn_1} + \varepsilon_{n_1 n_2} + \varepsilon_{n_2 q})/c$  are the travel times of the waves through the link  $T_p - R_q$ ,  $T_p - s^{(n_i)} - R_q$ , and  $T_p - s^{(n_1)} - s^{(n_2)} - R_q$ , respectively. Here,  $c$  is the speed of light and  $I = 3$ . The symbols  $K_{pq}$  and  $\Omega_{pq}$  designate the Ricean factor and the total power of the  $T_p - R_q$  link, respectively. Parameters  $\eta_{SB_i}$  and  $\eta_{DB}$  specify how much the single- and double-bounced rays contribute to the total scattered power  $\Omega_{pq}/(K_{pq} + 1)$ . Note that these energy-related parameters satisfy  $\sum_{i=1}^I \eta_{SB_i} + \eta_{DB} = 1$ . The phases  $\psi_{n_i}$  and  $\psi_{n_1, n_2}$  are independent and identically distributed (i.i.d.) random variables with uniform distributions over  $[-\pi, \pi)$ ,  $f_{Tmax}$  and  $f_{Rmax}$  are the maximum Doppler frequencies with respect to the Tx and Rx, respectively. Note that the AoD  $\phi_T^{(n_i)}$  and AoA  $\phi_R^{(n_i)}$  are independent for double-bounced rays, while they are interdependent for single-bounced rays.

From Fig. 1 and based on the application of the law of cosines in appropriate triangles, the distances  $\varepsilon_{pq}$ ,  $\varepsilon_{pn_i}$ ,  $\varepsilon_{n_i q}$ , and  $\varepsilon_{n_1 n_2}$  in (2)–(4) for any scenario (macro-cell ( $D \geq 1000$  m), micro-cell ( $300 < D < 1000$  m), or pico-cell ( $D \leq 300$  m) scenario) can be expressed as

$$\varepsilon_{pq} \approx \varepsilon - k_q \delta_R \cos(\phi_{R_q}^{LoS} - \beta_R) \quad (5)$$

$$\varepsilon_{pn_1} \approx R_T - k_p \delta_T \cos(\phi_T^{(n_1)} - \beta_T) \quad (6)$$

$$\varepsilon_{n_1 q} \approx \xi_{n_1} - k_q \delta_R \cos(\phi_R^{(n_1)} - \beta_R) \quad (7)$$

$$\varepsilon_{pn_2} \approx \xi_{n_2} - k_p \delta_T \cos(\phi_T^{(n_2)} - \beta_T) \quad (8)$$

$$\varepsilon_{n_2 q} \approx R_R - k_q \delta_R \cos(\phi_R^{(n_2)} - \beta_R) \quad (9)$$

$$\varepsilon_{pn_3} \approx \xi_T^{(n_3)} - k_p \delta_T \cos(\phi_T^{(n_3)} - \beta_T) \quad (10)$$

$$\varepsilon_{n_3 q} \approx \xi_R^{(n_3)} - k_q \delta_R \cos(\phi_R^{(n_3)} - \beta_R) \quad (11)$$

$$\varepsilon_{n_1 n_2} \approx D - R_T \cos \phi_T^{(n_1)} + R_R \cos \phi_R^{(n_2)} \quad (12)$$

where  $\phi_{R_q}^{LoS} \approx \pi$ ,  $\varepsilon \approx D - k_p \delta_T \cos \beta_T$ ,  $\xi_{n_1} = (D^2 + R_T^2 - 2D \times R_T \cos \phi_T^{(n_1)})^{-1/2}$ ,  $\xi_{n_2} = \sqrt{D^2 + R_R^2 + 2DR_R \cos \phi_R^{(n_2)}}$ ,  $\xi_T^{(n_3)} = (a^2 + f^2 + 2af \cos \phi_R^{(n_3)})/(a + f \cos \phi_R^{(n_3)})$ ,  $\xi_R^{(n_3)} = b^2/(a + f \cos \phi_R^{(n_3)})$ ,  $k_p = (M_T - 2p + 1)/2$ , and  $k_q = (M_R - 2q + 1)/2$ . Here  $b$  denotes the semi-minor axis of the ellipse and the equality  $a^2 = b^2 + f^2$  holds. As shown in Appendix A, based on the newly proposed general method to derive the exact relationship between the AoA and AoD for any shape of the scattering region, we have

$$\sin \phi_R^{(n_1)} = \frac{R_T \sin \phi_T^{(n_1)}}{\sqrt{R_T^2 + D^2 - 2R_T D \cos \phi_T^{(n_1)}}} \quad (13)$$

$$\cos \phi_R^{(n_1)} = \frac{-D + R_T \cos \phi_T^{(n_1)}}{\sqrt{R_T^2 + D^2 - 2R_T D \cos \phi_T^{(n_1)}}} \quad (14)$$

$$\sin \phi_T^{(n_2)} = \frac{R_R \sin \phi_R^{(n_2)}}{\sqrt{R_R^2 + D^2 + 2R_R D \cos \phi_R^{(n_2)}}} \quad (15)$$

$$\cos \phi_T^{(n_2)} = \frac{D + R_R \cos \phi_R^{(n_2)}}{\sqrt{R_R^2 + D^2 + 2R_R D \cos \phi_R^{(n_2)}}} \quad (16)$$

$$\sin \phi_T^{(n_3)} = \frac{b^2 \sin \phi_R^{(n_3)}}{a^2 + f^2 + 2af \cos \phi_R^{(n_3)}} \quad (17)$$

$$\cos \phi_T^{(n_3)} = \frac{2af + (a^2 + f^2) \cos \phi_R^{(n_3)}}{a^2 + f^2 + 2af \cos \phi_R^{(n_3)}}. \quad (18)$$

Note that the above derived expressions in (5)–(18) are sufficiently general and suitable for various scenarios. For macro- and micro-cell scenarios, the assumption  $D \gg \max\{R_T, R_R\}$ , which is invalid for pico-cell scenarios, is fulfilled. Then, the general expressions of  $\xi_{n_1}$  and  $\xi_{n_2}$  can further reduce to the widely used approximate expressions as  $\xi_{n_1} \approx D - R_T \cos \phi_T^{(n_1)}$  and  $\xi_{n_2} \approx D + R_R \cos \phi_R^{(n_2)}$ , respectively. In addition, the general expressions (13)–(16) for the two-ring model can further reduce to the widely used approximate expressions as  $\phi_R^{(n_1)} \approx \pi - \Delta_T \sin \phi_T^{(n_1)}$  and  $\phi_T^{(n_2)} \approx \Delta_R \sin \phi_R^{(n_2)}$  with  $\Delta_T \approx R_T/D$  and  $\Delta_R \approx R_R/D$ . Moreover, the relationships (17) and (18) for the ellipse model obtained by using our method significantly simplify the relationships derived based on pure ellipse properties, such as (A1)–(A3) in [20] and (27), (28), and (32) in [21].

Since the number of effective scatterers are assumed to be infinite, i.e.,  $N_i \rightarrow \infty$ , the proposed model in (1) is actually a mathematical reference model and results in the Ricean PDF. Due to the infinite complexity, a reference model cannot be implemented in practice. However, as mentioned in [22], a reference model can be used for theoretical analysis and design of a communication system, and also is a starting point to design a realizable simulation model that has the reasonable complexity, i.e., finite values of  $N_i$ . For our reference model, the discrete expressions of the AoA,  $\phi_R^{(n_i)}$ , and AoD,  $\phi_T^{(n_i)}$ , can be replaced by the continuous expressions  $\phi_R^{(SB_i)}$  and  $\phi_T^{(SB_i)}$ , respectively. In the literature, many different distributions have been proposed to characterize AoD  $\phi_T^{(SB_i)}$  and AoA  $\phi_R^{(SB_i)}$ , such as the uniform, Gaussian, wrapped Gaussian, and cardioid PDFs [18]. In this paper, the von Mises PDF [23] is used, which can approximate all the aforementioned PDFs. The von Mises PDF is defined as  $f(\phi) \triangleq \exp[k \cos(\phi - \mu)] / [2\pi I_0(k)]$ , where  $\phi \in [-\pi, \pi)$ ,  $I_0(\cdot)$  is the zeroth-order modified Bessel function of the first kind,  $\mu \in [-\pi, \pi)$  accounts for the mean value of the angle  $\phi$ , and  $k$  ( $k \geq 0$ ) is a real-valued parameter that controls the angle spread of the angle  $\phi$ .

As mentioned in the introduction, the proposed model in (1) is adaptable to a wide variety of M2M propagation environments by adjusting model parameters. It turns out that these important model parameters are the energy-related parameters  $\eta_{SB_i}$  and  $\eta_{DB}$ , and the Ricean factor  $K_{pq}$ . For a macro-cell scenario, the Ricean factor  $K_{pq}$  and the energy parameter  $\eta_{SB_3}$  related to the single-bounce ellipse model are very small or even close to zero. The received signal power mainly comes from single- and double-bounced rays of the two-ring model, in which we assume that double-bounced rays bear more energy than single-bounced rays due to the large distance  $D$  (larger distance  $D$  results in the independence of the AoD and AoA), i.e.,  $\eta_{DB} > \max\{\eta_{SB_1}, \eta_{SB_2}\} \gg \eta_{SB_3}$ . This

means that a macro-cell scenario can be well characterized by using a two-ring model with a negligible LoS component. In contrast to macro-cell scenarios, in micro- and pico-cell scenarios, the VTD significantly affects the channel characteristics as presented in [8]. To consider the impact of the VTD on channel statistics, we need to distinguish between the moving cars around the Tx and Rx and the stationary roadside environments (e.g., buildings, trees, parked cars, etc.). Therefore, we use a two-ring model to mimic the moving cars and an ellipse model to depict the stationary roadside environments. Note that ellipse models have been widely used to model F2M channels in micro- and pico-cell scenarios [20], [21]. However, to the best of the authors' knowledge, this is the first time that an ellipse model is used to mimic M2M channels. For a low VTD, the value of  $K_{pq}$  is large since the LoS component can bear a significant amount of power. Also, the received scattered power is mainly from waves reflected by the stationary roadside environments described by the scatterers located on the ellipse. The moving cars represented by the scatterers located on the two rings are sparse and thus more likely to be single-bounced, rather than double-bounced. This indicates that  $\eta_{SB_3} > \max\{\eta_{SB_1}, \eta_{SB_2}\} > \eta_{DB}$  holds. For a high VTD, the value of  $K_{pq}$  is smaller than that in the low VTD scenario. Also, due to the large amount of moving cars, the double-bounced rays of the two-ring model bear more energy than single-bounced rays of two-ring and ellipse models, i.e.,  $\eta_{DB} > \max\{\eta_{SB_1}, \eta_{SB_2}, \eta_{SB_3}\}$ . Therefore, a micro-cell and pico-cell scenario with consideration of the VTD can be well characterized by utilizing a combined two-ring model and ellipse model with a LoS component.

### III. NEW GENERIC STF CF AND SDF PSD

In this section, based on the proposed channel model in (1), we will derive the STF CF and the corresponding SDF PSD for a non-isotropic scattering environment.

#### A. New Generic STF CF

Under the wide sense stationary (WSS) condition, the normalized STF CF between any two complex fading envelopes  $h_{pq}(t)$  and  $h'_{p'q'}(t)$  with different carrier frequencies  $f_c$  and  $f'_c$ , respectively, is defined as [24]

$$\rho_{h_{pq}h'_{p'q'}}(\tau, \chi) = \frac{\mathbf{E} [h_{pq}(t) h'^*_{p'q'}(t - \tau)]}{\sqrt{\Omega_{pq}\Omega_{p'q'}}} = \rho_{h_{pq}^{LoS}h'_{p'q'}^{LoS}}(\tau, \chi) + \sum_{i=1}^I \rho_{h_{pq}^{SB_i}h'_{p'q'}^{SB_i}}(\tau, \chi) + \rho_{h_{pq}^{DB}h'_{p'q'}^{DB}}(\tau, \chi) \quad (19)$$

where  $(\cdot)^*$  denotes the complex conjugate operation,  $\mathbf{E}[\cdot]$  is the statistical expectation operator,  $p, p' \in \{1, 2, \dots, M_T\}$ , and  $q, q' \in \{1, 2, \dots, M_R\}$ . It should be observed that (19) is a function of time separation  $\tau$ , space separation  $\delta_T$  and  $\delta_R$ , and frequency separation  $\chi = f'_c - f_c$ . Note that the CF definition in (19) is different from the following definition widely used in other references, e.g., [13], [14], [17], [18]

$$\tilde{\rho}_{h_{pq}h'_{p'q'}}(\tau, \chi) = \mathbf{E} [h_{pq}(t) h'^*_{p'q'}(t + \tau)] / \sqrt{\Omega_{pq}\Omega_{p'q'}}. \quad (20)$$

The CF definition in (19) is actually the correct one following the CF definition given in Stochastic Processes (see Equation

(9-51) in [19]). It can easily be shown that the expression (20) equals the complex conjugate of the correct CF in (19), i.e.,  $\tilde{\rho}_{h_{pq}h'_{p'q'}}(\tau, \chi) = \rho_{h_{pq}h'_{p'q'}}^*(\tau, \chi)$ , and thus is an incorrect definition. Only when  $\rho_{h_{pq}h'_{p'q'}}^*(\tau, \chi)$  is a real function (no imaginary part),  $\tilde{\rho}_{h_{pq}h'_{p'q'}}(\tau, \chi) = \rho_{h_{pq}h'_{p'q'}}(\tau, \chi)$  holds.

Substituting (2) and (5) into (19), we can obtain the STF CF of the LoS component as

$$\rho_{h_{pq}^{LoS}h'_{p'q'}^{LoS}}(\tau) = \sqrt{\frac{K_{pq}K_{p'q'}}{(K_{pq}+1)(K_{p'q'}+1)}} e^{j2\pi(G_1+\tau H_1+\frac{\chi}{c}L_1)} \quad (21)$$

where  $G_1 = P \cos \beta_T - Q \cos \beta_R$ ,  $H_1 = f_{T_{max}} \cos \gamma_T - f_{R_{max}} \cos \gamma_R$ , and  $L_1 = D - k_{p'} \delta_T \cos \beta_T + k_{q'} \delta_R \cos \beta_R$  with  $P = (p' - p) \delta_T / \lambda$ ,  $Q = (q' - q) \delta_R / \lambda$ ,  $k_{p'} = (M_T - 2p' + 1) / 2$ , and  $k_{q'} = (M_R - 2q' + 1) / 2$ .

Applying the von Mises PDF to the two-ring model, we obtain  $f(\phi_T^{SB_1}) = \exp[k_T^{TR} \cos(\phi_T^{SB_1} - \mu_T^{TR})] / [2\pi I_0(k_T^{TR})]$  for the AoD  $\phi_T^{SB_1}$  and  $f(\phi_R^{SB_2}) = \exp[k_R^{TR} \cos(\phi_R^{SB_2} - \mu_R^{TR})] / [2\pi I_0(k_R^{TR})]$  for the AoA  $\phi_R^{SB_2}$ . Substituting (3) and (6)–(9) into (19), we can express the STF CF of the single-bounce two-ring model as

$$\rho_{h_{pq}^{SB_1(2)}h'_{p'q'}^{SB_1(2)}}(\tau, \chi) = \frac{\eta_{SB_1(2)}}{2\pi I_0(k_T^{TR}) \sqrt{(K_{pq}+1)(K_{p'q'}+1)}} \times \int_{-\pi}^{\pi} e^{k_T^{TR} \cos(\phi_T^{SB_1(2)} - \mu_T^{TR})} e^{j2\pi(G_2+\tau H_2+\frac{\chi}{c}L_2)} d\phi_T^{SB_1(2)} \quad (22)$$

where  $G_2 = P \cos(\phi_T^{SB_1(2)} - \beta_T) + Q \cos(\phi_R^{SB_1(2)} - \beta_R)$ ,  $H_2 = f_{T_{max}} \cos(\phi_T^{SB_1(2)} - \gamma_T) + f_{R_{max}} \cos(\phi_R^{SB_1(2)} - \gamma_R)$ , and  $L_2 = R_{T(R)} + \xi_{n_1(2)} - k_{p'} \delta_T \cos(\phi_T^{SB_1(2)} - \beta_T) - k_{q'} \delta_R \cos(\phi_R^{SB_1(2)} - \beta_R)$  with the parameters  $\sin \phi_R^{SB_1}$ ,  $\cos \phi_R^{SB_1}$ ,  $\sin \phi_T^{SB_2}$ , and  $\cos \phi_T^{SB_2}$  following the expressions in (13)–(16), respectively. For the macro- and micro-cell scenarios, (22) can be further simplified as the following closed-form expression

$$\rho_{h_{pq}^{SB_1(2)}h'_{p'q'}^{SB_1(2)}}(\tau, \chi) = \eta_{SB_1(2)} e^{jC_{T(R)}^{SB_1(2)}} \times \frac{I_0 \left\{ \sqrt{(A_{T(R)}^{SB_1(2)})^2 + (B_{T(R)}^{SB_1(2)})^2} \right\}}{\sqrt{(K_{pq}+1)(K_{p'q'}+1)} I_0(k_T^{TR})} \quad (23)$$

where

$$A_{T(R)}^{SB_1(2)} = k_T^{TR} \cos \mu_T^{TR} + j2\pi\tau f_{T(R)_{max}} \cos \gamma_{T(R)} + j2\pi P(Q) \cos \beta_{T(R)} - j2\pi\chi X_{A_{T(R)}} / c \quad (24a)$$

$$B_{T(R)}^{SB_1(2)} = k_T^{TR} \sin \mu_T^{TR} + j2\pi\tau (f_{T(R)_{max}} \sin \gamma_{T(R)} + f_{R(T)_{max}} \Delta_{T(R)} \sin \gamma_{R(T)} + j2\pi(P(Q) \sin \beta_{T(R)} + Q(P) \Delta_{T(R)} \sin \beta_{R(T)} - \chi X_{B_{T(R)}} / c) \quad (24b)$$

$$C_{T(R)}^{SB_1(2)} = \mp 2\pi\tau f_{R(T)_{max}} \cos \gamma_{R(T)} \mp 2\pi Q(P) \cos \beta_{R(T)} + 2\pi\chi X_{C_{T(R)}} / c \quad (24c)$$

with  $X_{A_T} = R_T - k_{p'} \delta_T \cos \beta_T$ ,  $X_{B_T} = -k_{p'} \delta_T \sin \beta_T - k_{q'} \delta_R \Delta_T \sin \beta_R$ ,  $X_{C_T} = R_T + D - k_{q'} \delta_R \cos \beta_R$ ,  $X_{A_R} = -R_R - k_{q'} \delta_R \cos \beta_R$ ,  $X_{B_R} = -k_{q'} \delta_R \sin \beta_R - k_{p'} \delta_T \Delta_R \sin \beta_T$ , and  $X_{C_R} = R_R + D + k_{p'} \delta_T \cos \beta_T$ .

Applying the von Mises PDF to the ellipse model, we get  $f(\phi_R^{SB_3}) = \exp[k_R^{EL} \cos(\phi_R^{SB_3} - \mu_R^{EL})] / [2\pi I_0(k_R^{EL})]$ . Performing the substitution of (3), (10), and (11) into (19), we can obtain the STF CF of the single-bounce ellipse model as

$$\rho_{h_{pq}^{SB_3}h'_{p'q'}^{SB_3}}(\tau, \chi) = \frac{\eta_{SB_3}}{2\pi I_0(k_R^{EL}) \sqrt{(K_{pq}+1)(K_{p'q'}+1)}} \times \int_{-\pi}^{\pi} e^{k_R^{EL} \cos(\phi_R^{SB_3} - \mu_R^{EL})} e^{j2\pi(G_3+\tau H_3+\frac{\chi}{c}L_3)} d\phi_R^{SB_3} \quad (25)$$

where  $G_3 = P \cos(\phi_T^{SB_3} - \beta_T) + Q \cos(\phi_R^{SB_3} - \beta_R)$ ,  $H_3 = f_{T_{max}} \cos(\phi_T^{SB_3} - \gamma_T) + f_{R_{max}} \cos(\phi_R^{SB_3} - \gamma_R)$ , and  $L_3 = 2a - k_{p'} \delta_T \cos(\phi_T^{SB_3} - \beta_T) - k_{q'} \delta_R \cos(\phi_R^{SB_3} - \beta_R)$  with the parameters  $\sin \phi_T^{SB_3}$  and  $\cos \phi_T^{SB_3}$  following the expressions in (17) and (18), respectively.

The substitution of (4), (6), (9), and (12) into (19) results in the following STF CF for the double-bounce two-ring model

$$\rho_{h_{pq}^{DB}h'_{p'q'}^{DB}}(\tau, \chi) = \eta_{DB} e^{jC^{DB}} \frac{I_0 \left\{ \sqrt{(A_T^{DB})^2 + (B_T^{DB})^2} \right\}}{\sqrt{(K_{pq}+1)(K_{p'q'}+1)}} \times \frac{I_0 \left\{ \sqrt{(A_R^{DB})^2 + (B_R^{DB})^2} \right\}}{I_0(k_T^{TR}) I_0(k_R^{TR})} \quad (26)$$

where

$$C^{DB} = 2\pi\chi (R_T + R_R + D) / c \quad (27a)$$

$$A_{T(R)}^{DB} = k_{T(R)}^{TR} \cos \mu_{T(R)}^{TR} + j2\pi\tau f_{T(R)_{max}} \cos \gamma_{T(R)} + j2\pi P(Q) \cos \beta_{T(R)} \mp j2\pi\chi (R_{T(R)} \mp k_{p'}(q') \cos \beta_{T(R)}) / c \quad (27b)$$

$$B_{T(R)}^{DB} = k_{T(R)}^{TR} \sin \mu_{T(R)}^{TR} + j2\pi\tau f_{T(R)_{max}} \sin \gamma_{T(R)} + j2\pi P(Q) \sin \beta_{T(R)} + j2\pi\chi k_{p'}(q') \sin \beta_{T(R)} / c. \quad (27c)$$

Since the derivations of (21)–(23), (25), and (26) are similar, only the brief outline of the derivation of (23) is given in Appendix B, while others are omitted for brevity.

The derived STF CF in (19) includes many existing CFs as special cases. If we only consider the two-ring model ( $\eta_{SB_3} = 0$ ) for a M2M channel in a macro- or micro-cell scenario ( $D \gg \max\{R_T, R_R\}$ ) with the frequency separation  $\chi = 0$ , then the CF in (19) will be reduced to the CF in (18) of [14], where the time separation  $\tau$  should be replaced by  $-\tau$  since the CF definition (20) is used in [14]. Consequently, the derived STF CF in (19) also includes other CFs listed in [14] as special cases, when  $\tau$  is replaced by  $-\tau$ . If we consider the one-ring model only around the Rx for a F2M channel in a macro-cell scenario ( $\eta_{SB_1} = \eta_{SB_3} = \eta_{DB} = f_{T_{max}} = 0$ ) with non-LoS (NLoS) condition ( $K_{pq} = 0$ ), the derived STF CF in (19) includes the CF (6) in [18] and, subsequently, other CFs listed in [18] as special cases, when  $\tau$  is replaced by  $-\tau$ . Furthermore, the CF (7) in [24] can be obtained from (19) with  $K_{pq} = f_{T_{max}} = \chi = \eta_{SB_3} = \eta_{DB} = 0$ . Consequently, other CFs listed in [24] can also be obtained from (19).

### B. New Generic SDF PSD

Applying the Fourier transform to the STF CF in (19) in terms of  $\tau$ , we can obtain the corresponding SDF PSD as

$$S_{h_{pq}h'_{p'q'}}(f_D, \chi) = \int_{-\infty}^{\infty} \rho_{h_{pq}h'_{p'q'}}(\tau, \chi) e^{-j2\pi f_D \tau} d\tau$$

$$= S_{h_{pq}^{LoS}h'_{p'q'}^{LoS}}(f_D, \chi) + \sum_{i=1}^I S_{h_{pq}^{SB_i}h'_{p'q'}^{SB_i}}(f_D, \chi) + S_{h_{pq}^{DB}h'_{p'q'}^{DB}}(f_D, \chi) \quad (28)$$

where  $f_D$  is the Doppler frequency. The integral in (28) must be evaluated numerically in the case of the single-bounce two-ring and ellipse models. Whereas for other cases, we can obtain the following closed-form solutions.

1) In the case of the LoS component, substituting (21) into (28) we have

$$S_{h_{pq}^{LoS}h'_{p'q'}^{LoS}}(f_D, \chi) = \sqrt{\frac{K_{pq}K_{p'q'}}{(K_{pq}+1)(K_{p'q'}+1)}} \times e^{j2\pi(G_1 + \frac{\chi}{c}L_1)} \delta(f_D - H_1) \quad (29)$$

where  $\delta(\cdot)$  denotes the Dirac delta function.

2) In terms of the single-bounce two-ring model for macro- and micro-cell scenarios, substituting (23) into (28) we have

$$S_{h_{pq}^{SB_1(2)}h'_{p'q'}^{SB_1(2)}}(f_D, \chi) = \frac{\eta_{SB_1(2)} 2e^{jU_{T(R)}^{SB_1(2)}}}{I_0(k_{T(R)}^{TR})}$$

$$e^{jO_{T(R)}^{SB_1(2)} \frac{D_{T(R)}^{SB_1(2)}}{W_{T(R)}^{SB_1(2)}}} \cos\left(\frac{E_{T(R)}^{SB_1(2)}}{W_{T(R)}^{SB_1(2)}} \sqrt{W_{T(R)}^{SB_1(2)} - (O_{T(R)}^{SB_1(2)})^2}\right)$$

$$\times \frac{1}{\sqrt{(K_{pq}+1)(K_{p'q'}+1)} \sqrt{W_{T(R)}^{SB_1(2)} - (O_{T(R)}^{SB_1(2)})^2}} \quad (30)$$

where  $O_{T(R)}^{SB_1(2)} = 2\pi(f_D \pm f_{R(T)max} \cos \gamma_{R(T)})$

$$U_{T(R)}^{SB_1(2)} = \mp 2\pi Q(P) \cos \beta_{R(T)} + 2\pi \chi (R_{T(R)} + D \pm k_{q'(p')} \delta_{R(T)} \times \cos \beta_{R(T)}) / c \quad (31a)$$

$$W_{T(R)}^{SB_1(2)} = 4\pi^2 f_{T(R)max}^2 + 4\pi^2 f_{R(T)max}^2 \Delta_{T(R)}^2 \sin^2 \gamma_{R(T)} + 8\pi^2 \times f_{Tmax} f_{Rmax} \Delta_{T(R)} \sin \gamma_T \sin \gamma_R \quad (31b)$$

$$D_{T(R)}^{SB_1(2)} = -j2\pi k_{T(R)}^{TR} J_{T(R)} + 4\pi^2 P(Q) (f_{T(R)max} \cos(\beta_{T(R)} - \gamma_{T(R)}) + \Delta_{T(R)} f_{R(T)max} \sin \beta_{T(R)} \sin \gamma_{R(T)}) + 4\pi^2 Q(P) \times (\Delta_{T(R)} f_{T(R)max} \sin \beta_{R(T)} \sin \gamma_{T(R)} + \Delta_{T(R)}^2 f_{R(T)max} \times \sin \beta_{R(T)} \sin \gamma_{R(T)}) - 4\pi^2 \chi (f_{T(R)max} Y_{TD_{T(R)}} + f_{R(T)max} \times \Delta_{T(R)} \sin \gamma_{R(T)} Y_{RD_{T(R}})) / c \quad (31c)$$

$$E_{T(R)}^{SB_1(2)} = -j2\pi k_{T(R)}^{TR} (f_{T(R)max} \sin(\gamma_{T(R)} - \mu_{T(R)}^{TR}) + f_{R(T)max} \times \Delta_{T(R)} \sin \gamma_{R(T)} \cos \mu_{T(R)}^{TR}) - 4\pi^2 P(Q) (f_{T(R)max} \sin(\beta_{T(R)} - \gamma_{T(R)}) - \Delta_{T(R)} f_{R(T)max} \cos \beta_{T(R)} \sin \gamma_{R(T)}) - 4\pi^2 Q(P) \Delta_{T(R)} \times f_{T(R)max} \sin \beta_{R(T)} \cos \gamma_{T(R)} - 4\pi^2 \chi (f_{T(R)max} Y_{TE_{T(R)}} + f_{R(T)max} \Delta_{T(R)} \sin \gamma_{R(T)} Y_{RE_{T(R}})) / c \quad (31d)$$

with

$$J_{T(R)} = f_{T(R)max} \cos(\gamma_{T(R)} - \mu_{T(R)}^{TR}) - f_{R(T)max} \Delta_{T(R)} \sin \gamma_{R(T)} \times \sin \mu_{T(R)}^{TR} \quad (32a)$$

$$Y_{TD_{T(R)}} = \pm R_{T(R)} \cos \gamma_{T(R)} - k_{p'(q')} \delta_{T(R)} \cos(\beta_{T(R)} - \gamma_{T(R)}) - k_{q'(p')} \delta_{R(T)} \Delta_{T(R)} \sin \beta_{R(T)} \sin \gamma_{T(R)} \quad (32b)$$

$$Y_{TE_{T(R)}} = \pm R_{T(R)} \sin \gamma_{T(R)} + k_{p'(q')} \delta_{T(R)} \sin(\beta_{T(R)} \mp \gamma_{T(R)}) + k_{q'(p')} \delta_{R(T)} \Delta_{T(R)} \sin \beta_{R(T)} \cos \gamma_{T(R)} \quad (32c)$$

$$Y_{RD_{T(R)}} = -k_{p'(q')} \delta_{T(R)} \sin \beta_{T(R)} - k_{q'(p')} \delta_{R(T)} \Delta_{T(R)} \sin \beta_{R(T)} \quad (32d)$$

$$Y_{RE_{T(R)}} = \pm R_{T(R)} - k_{p'(q')} \delta_{T(R)} \cos \beta_{T(R)}. \quad (32e)$$

For the Doppler PSD in (30), the range of Doppler frequencies is limited by  $|f_D + f_{Rmax} \cos \gamma_R| \leq \sqrt{W_T^{SB_1} / (2\pi)}$  and  $|f_D - f_{Tmax} \cos \gamma_T| \leq \sqrt{W_R^{SB_2} / (2\pi)}$ . Note that the expression of (30) corrects the ones of (40) and (41) in [14].

3) In the case of the double-bounce two-ring model, substituting (26) into (28) we have

$$S_{h_{pq}^{DB}h'_{p'q'}^{DB}}(f_D, \chi) = \frac{\eta_{DB} e^{jC^{DB}}}{\sqrt{(K_{pq}+1)(K_{p'q'}+1)} I_0(k_{T(R)}^{TR}) I_0(k_{R(R)}^{TR})} \times 2e^{jO_{T(R)}^{DB} \frac{D_{T(R)}^{DB}}{W_{T(R)}^{DB}} \cos\left(\frac{E_{T(R)}^{DB}}{W_{T(R)}^{DB}} \sqrt{W_{T(R)}^{DB} - (O_{T(R)}^{DB})^2}\right)} \sqrt{W_{T(R)}^{DB} - (O_{T(R)}^{DB})^2} \odot 2e^{jO_{R(R)}^{DB} \frac{D_{R(R)}^{DB}}{W_{R(R)}^{DB}} \cos\left(\frac{E_{R(R)}^{DB}}{W_{R(R)}^{DB}} \sqrt{W_{R(R)}^{DB} - (O_{R(R)}^{DB})^2}\right)} \sqrt{W_{R(R)}^{DB} - (O_{R(R)}^{DB})^2} \quad (33)$$

where  $\odot$  denotes convolution,  $O^{DB} = 2\pi f_D$ ,  $W_{T(R)}^{DB} = 4\pi^2 f_{T(R)max}^2$

$$D_{T(R)}^{DB} = 4\pi^2 P(Q) f_{T(R)max} \cos(\beta_{T(R)} - \gamma_{T(R)}) - j2\pi k_{T(R)}^{TR} \times f_{T(R)max} \cos(\gamma_{T(R)} - \mu_{T(R)}^{TR}) - \frac{4\pi^2 \chi f_{T(R)max} Y_{DT(R)}}{c} \quad (34a)$$

$$E_{T(R)}^{DB} = \pm 4\pi^2 P(Q) f_{T(R)max} \sin(\beta_{T(R)} - \gamma_{T(R)}) \pm j2\pi k_{T(R)}^{TR} \times f_{T(R)max} \sin(\gamma_{T(R)} - \mu_{T(R)}^{TR}) + \frac{4\pi^2 \chi f_{T(R)max} Y_{ET(R)}}{c} \quad (34b)$$

with  $Y_{DT} = R_T \cos \gamma_T - k_{p'} \delta_T \cos(\beta_T - \gamma_T)$ ,  $Y_{ET} = R_T \sin \gamma_T + k_{p'} \delta_T \sin(\beta_T - \gamma_T)$ ,  $Y_{DR} = -R_R \cos \gamma_R - k_{q'} \delta_R \cos(\beta_R - \gamma_R)$ , and  $Y_{ER} = -R_R \sin \gamma_R + k_{q'} \delta_R \sin(\beta_R - \gamma_R)$ . For the Doppler PSD in (33), the range of Doppler frequencies is limited by  $|f_D| \leq f_{T_{max}} + f_{R_{max}}$ . Due to the similar derivations of (29), (30), and (33), Appendix C only gives the brief outline of the derivation of (30), while others are omitted here.

Many existing Doppler PSDs are special cases of the derived SDF PSD in (28). The simplest case is Clarke's Doppler PSD  $1 / (2\pi f_D \sqrt{1 - (f_D / f_{R_{max}})^2})$  ( $|f_D| \leq f_{R_{max}}$ ) [22], which can be obtained from (28) by setting  $K_{pq} = 0$  (NLoS condition),  $k_R^{TR} = 0$  (isotropic scattering around the Rx),  $\chi = 0$  (no frequency separation),  $f_{T_{max}} = \eta_{SB_1} = \eta_{SB_3} = \eta_{DB} = 0$  (fixed Tx, no scattering around the Tx), and applying  $D \gg \max\{R_T, R_R\}$  (macro- and micro-cell scenarios). The Doppler PSD for isotropic M2M fading channels presented as (41) in [11] can be obtained from (28) by setting  $K_{pq} = k_T^{TR} = k_R^{TR} = \delta_T = \delta_R = \chi = \eta_{SB_1} = \eta_{SB_2} = \eta_{SB_3} = 0$  and using  $D \gg \max\{R_T, R_R\}$ . Similarly, the space-Doppler PSD for non-isotropic double-bounce two-ring model shown as (42)<sup>1</sup> in [14] can be obtained from (28) by setting  $K_{pq} = \chi = \eta_{SB_1} = \eta_{SB_2} = \eta_{SB_3} = 0$  and utilizing  $D \gg \max\{R_T, R_R\}$ , when  $D_T^{TR}$  and  $D_R^{TR}$  are replaced by  $-D_T^{TR}$  and  $-D_R^{TR}$ , respectively, due to applying the different CF definitions.

To further demonstrate that the CF definition in (19) is correct, in Appendix D we compare the Doppler PSDs with different CFs (19) and (20). Appendix D demonstrates that (19) leads to the Doppler PSD capable of capturing the underlying physical phenomena of real channels for any scenarios, while the widely used expression (20) is only applicable to certain scenarios where the Doppler PSD is a real function and symmetrical to the origin (i.e., the corresponding CF is a real function), e.g., Clarke's scenario. In [13], [14], [17], [18], the commonly used formula (20) was misapplied to non-isotropic F2M or M2M scenarios.

#### IV. NUMERICAL RESULTS AND ANALYSIS

In this section, based on the derived STF CF and SDF PSD in Section III, the degenerate CFs and PSDs of MIMO M2M channels are numerically analyzed in detail. In addition, the normalized Doppler PSDs of the proposed model for different environments are given and some of them are compared with the available measured data in [6]. The following parameters are used for our numerical analysis:  $f_c = 5.9$  GHz,  $f_{T_{max}} = f_{R_{max}} = 570$  Hz,  $D = 300$  m,  $a = 200$  m, and  $R_T = R_R = 40$  m.

Figs. 2 and 3 illustrate the space and frequency CFs of the single- and double-bounce two-ring model and single-bounce ellipse model for different scenarios. It is obvious that both the space and frequency CFs vary significantly for different scenarios (Scenario *a* and Scenario *b*). We also notice that directions of motion (related to the values of  $\gamma_T$  and  $\gamma_R$ ) have no impact on the space and frequency CFs.

Fig. 4 shows normalized Doppler PSDs for different scenarios (Scenario *a* and Scenario *b*). For Scenario *a*, it is clear

<sup>1</sup>Note that the expression of (42) in [14] is inaccurate. The corrected expression should replace the terms  $-jk_T \cos(\gamma_T - \mu_T)$  and  $-jk_R \cos(\gamma_R - \mu_R)$  by  $+jk_T \cos(\gamma_T - \mu_T)$  and  $+jk_R \cos(\gamma_R - \mu_R)$ , respectively.

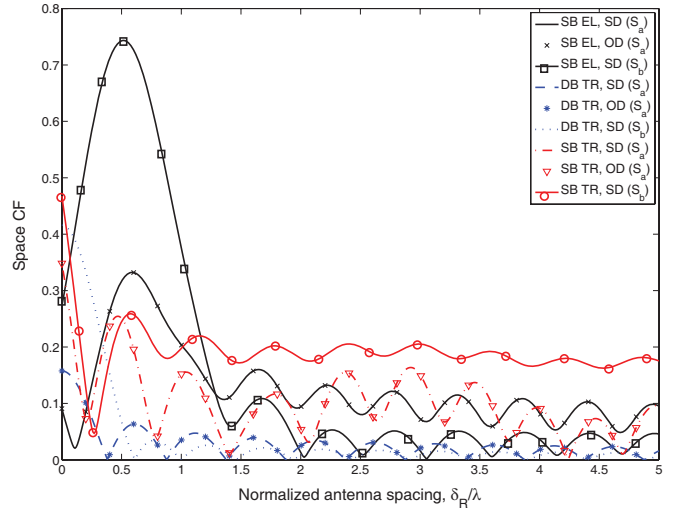


Fig. 2. Space CFs of the single-bounce (SB) ellipse (EL) model, double-bounce (DB) two-ring (TR) model, and SB TR model for different scenarios ( $\tau = 0$ ,  $\chi = 0$ , and  $\delta_T = 2$ ). SD: same direction ( $\gamma_T = \gamma_R = 0$ ); OD: opposite direction ( $\gamma_T = 0$  and  $\gamma_R = \pi$ ); Scenario *a* ( $S_a$ ):  $k_T^{TR} = k_R^{TR} = k_R^{EL} = 0$  (isotropic environments); Scenario *b* ( $S_b$ ):  $k_T^{TR} = k_R^{TR} = k_R^{EL} = 3$  (non-isotropic environments),  $\mu_T^{TR} = \pi/4$ , and  $\mu_R^{TR} = \mu_R^{EL} = 3\pi/4$ .

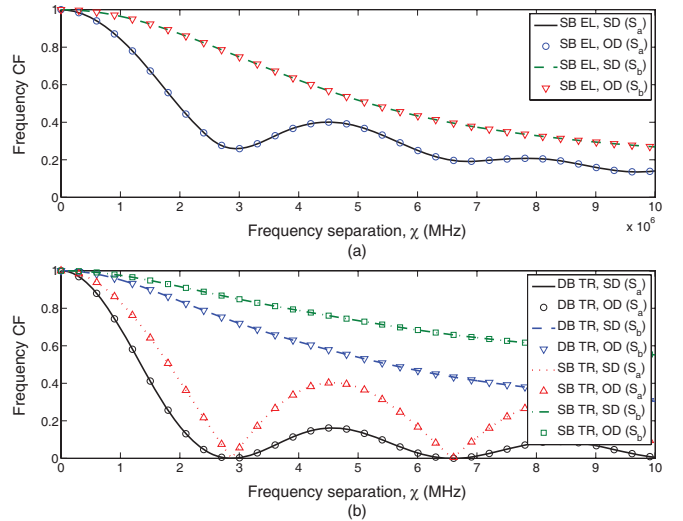


Fig. 3. Frequency CFs of the single-bounce (SB) ellipse (EL) model, double-bounce (DB) two-ring (TR) model, and SB TR model for different scenarios ( $\tau = 0$ ,  $\delta_T = \delta_R = 0$ ). SD: same direction ( $\gamma_T = \gamma_R = 0$ ); OD: opposite direction ( $\gamma_T = 0$  and  $\gamma_R = \pi$ ); Scenario *a* ( $S_a$ ):  $k_T^{TR} = k_R^{TR} = k_R^{EL} = 0$  (isotropic environments); Scenario *b* ( $S_b$ ):  $k_T^{TR} = k_R^{TR} = k_R^{EL} = 3$  (non-isotropic environments),  $\mu_T^{TR} = \pi/4$ , and  $\mu_R^{TR} = \mu_R^{EL} = 3\pi/4$ .

that no matter what the direction of motion (same or opposite) and the shape of the scattering region (one-ring, two-ring, or ellipse) are, the Doppler PSD of single-bounced rays is similar to the *U*-shaped PSD of F2M cellular channels<sup>2</sup>, whereas the Doppler PSD of double-bounced rays has “rounded”-shape having a peak in the middle. This indicates that the *U*-shaped Doppler PSD will appear when high dependency exists between the AoD and AoA, while the “rounded”-shaped Doppler PSD will appear when the AoD and AoA are relatively independent. We can also observe that for different directions

<sup>2</sup>Note that when the Tx and Rx move in the same direction, the Doppler PSD of the single-bounce ellipse model is not an exact *U*-shape, but it is reasonable to consider it as an approximate *U*-shape since peaks exist in both the left and right sides of the Doppler PSD instead of in the middle.

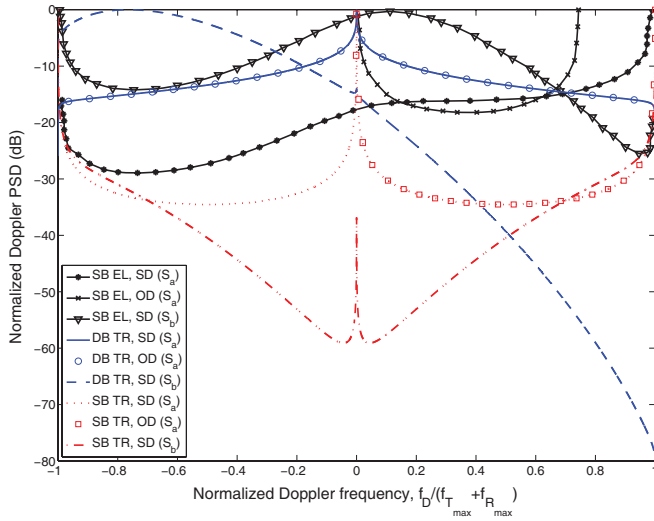


Fig. 4. Normalized Doppler PSDs of the single-bounce (SB) ellipse (EL) model, double-bounce (DB) two-ring (TR) model, and SB TR model for different scenarios ( $\delta_T = \delta_R = 0$ ,  $\chi = 0$ ). SD: same direction ( $\gamma_T = \gamma_R = 0$ ); OD: opposite direction ( $\gamma_T = 0$  and  $\gamma_R = \pi$ ); Scenario *a* ( $S_a$ ):  $k_T^{TR} = k_R^{TR} = k_R^{EL} = 0$  (isotropic environments); Scenario *b* ( $S_b$ ):  $k_T^{TR} = k_R^{TR} = k_R^{EL} = 3$  (non-isotropic environments),  $\mu_T^{TR} = \pi/4$ , and  $\mu_R^{TR} = \mu_R^{EL} = 3\pi/4$ .

of motion, the Doppler PSDs of double-bounced rays remain unchanged, while the Doppler PSDs of single-bounced rays change with different ranges of Doppler frequencies. More importantly, we found that the impact of single-bounced rays from different rings (ring around the Tx or Rx) on the Doppler PSD are the same for M2M channels when the Tx and Rx move in opposite directions, leading to the *U*-shaped Doppler PSD for the single-bounce two-ring model. When the Tx and Rx move in the same direction, the impact of single-bounced rays from different rings on the Doppler PSD are different in terms of the range of Doppler frequencies, which results in the double-*U*-shaped Doppler PSD for the single-bounce two-ring model. Therefore, we can conclude that a more realistic M2M channel model should take into account the different contributions from different rings. However, this has not been considered in all the existing M2M GBSMs, e.g., in [14]. It is worth mentioning that by setting one terminal fixed (i.e.,  $f_{Tmax} = 0$ ), our M2M model can reduce to a F2M model. In this case, we studied the Doppler PSD for the corresponding single- and double-bounce two-ring F2M models and single-bounce ellipse F2M model, and found that they have the same *U*-shaped PSD. For brevity, the results regarding F2M channels are omitted here. These observations indicate that the impact of single- and double-bounced rays on the Doppler PSD are completely different for M2M channels (*U*-shaped and “rounded”-shaped, respectively), while they are the same for F2M channels (*U*-shaped). At the end, the comparison of Scenario *a* and Scenario *b* illustrates the significant impact of angle spreads (related to the values of  $k_T^{TR}$ ,  $k_R^{TR}$ , and  $k_R^{EL}$ ) and mean angles (related to the values of  $\mu_T^{TR}$ ,  $\mu_R^{TR}$ , and  $\mu_R^{EL}$ ) on the Doppler PSD.

Figs. 5 and 6 depict the impact of the antenna element spacing and frequency separation on the Doppler PSD, respectively. Fig. 5 shows that the space separation introduces fluctuations in the Doppler PSD no matter what the shape of

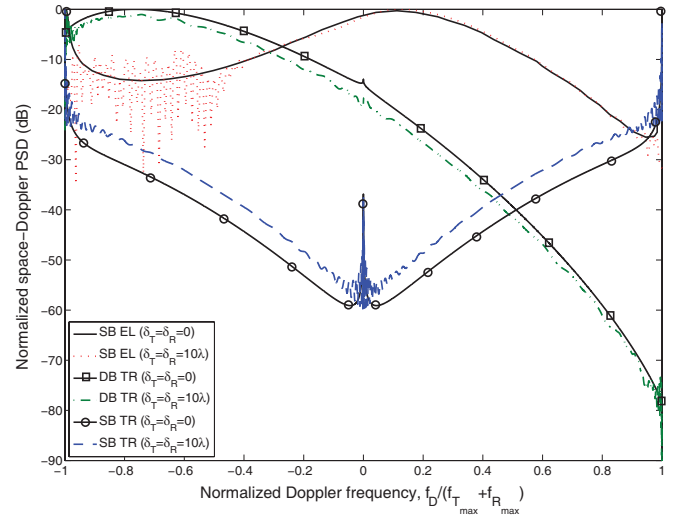


Fig. 5. Normalized space-Doppler PSDs of the single-bounce (SB) ellipse (EL) model, double-bounce (DB) two-ring (TR) model, and SB TR model for different antenna element spacings in a M2M non-isotropic scattering environment ( $k_T^{TR} = k_R^{TR} = k_R^{EL} = 3$ ,  $\mu_T^{TR} = \pi/4$ ,  $\mu_R^{TR} = \mu_R^{EL} = 3\pi/4$ ) with the Tx and Rx moving in the same direction ( $\gamma_T = \gamma_R = 0$ ).

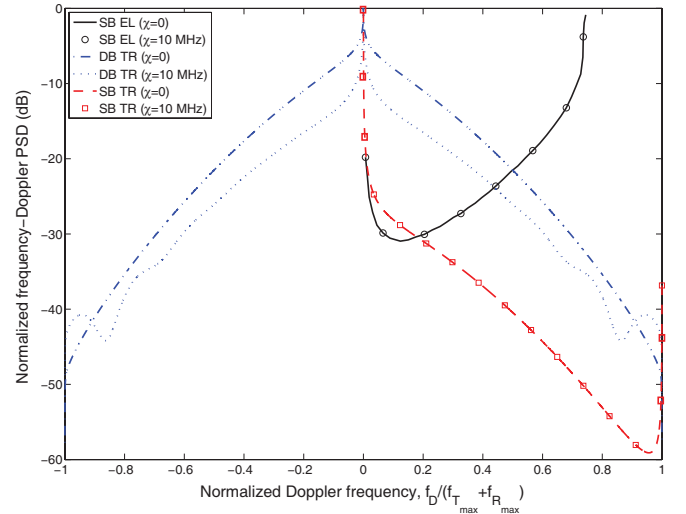


Fig. 6. Normalized frequency-Doppler PSDs of the single-bounce (SB) ellipse (EL) model, double-bounce (DB) two-ring (TR) model, and SB TR model for different frequency separations in a M2M non-isotropic scattering environment ( $k_T^{TR} = k_R^{TR} = k_R^{EL} = 3$ ,  $\mu_T^{TR} = \pi/4$ ,  $\mu_R^{TR} = \mu_R^{EL} = 3\pi/4$ ) with the Tx and Rx moving in the opposite direction ( $\gamma_T = 0$  and  $\gamma_R = \pi$ ).

the scattering region is. Fig. 6 illustrates that the frequency separation only generates fluctuations in the Doppler PSD for the double-bounce two-ring model, while for other cases, the impact of the frequency separation vanishes.

Figs. 7 (a) and (b) show the theoretical Doppler PSDs obtained from the proposed M2M model for different VTDs (low and high) when the Tx and Rx move in opposite directions and same direction, respectively. For further comparison, the measured data taken from Figs. 4 (a) and (c) in [6] are also plotted in Figs. 7 (a) and (b), respectively. In [6], the measurement campaigns were performed at a carrier frequency of 5.9 GHz on an expressway with a low VTD in the metropolitan Atlanta, Georgia area and the maximum Doppler frequencies were  $f_{Tmax} = f_{Rmax} = 570$  Hz. The distance between the Tx and Rx was approximately  $D = 300$  m and

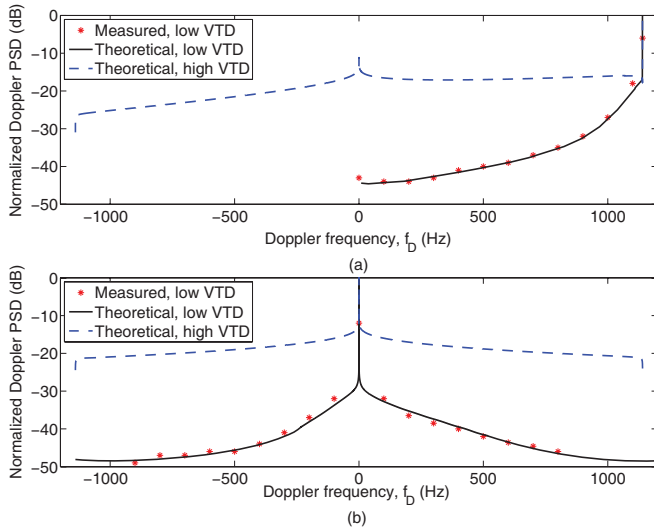


Fig. 7. Normalized Doppler PSDs of the proposed adaptive model for different SISO pico-cell scenarios ( $\delta_T = \delta_R = 0$ ,  $\chi = 0$ ): (a) Tx and Rx move in opposite directions, (b) Tx and Rx move in the same direction. VTD: vehicular traffic density.

the directions of movement were  $\gamma_T = 0$ ,  $\gamma_R = \pi$  (opposite direction, shown in Fig. 4 (a) in [6]) and  $\gamma_T = \gamma_R = 0$  (same direction, shown in Fig. 4 (c) in [6]). Both the Tx and Rx were equipped with one omnidirectional antenna, i.e., SISO case. Based on the measured scenarios in [6], we chose the following environment-related parameters:  $k_T^{TR} = 6.6$ ,  $k_R^{TR} = 8.3$ ,  $k_R^{EL} = 5.5$ ,  $\mu_T^{TR} = 12.8^\circ$ ,  $\mu_R^{TR} = 178.7^\circ$ , and  $\mu_R^{EL} = 131.6^\circ$  for Fig. 7 (a), and  $k_T^{TR} = 9.6$ ,  $k_R^{TR} = 3.6$ ,  $k_R^{EL} = 11.5$ ,  $\mu_T^{TR} = 21.7^\circ$ ,  $\mu_R^{TR} = 147.8^\circ$ , and  $\mu_R^{EL} = 171.6^\circ$  for Fig. 7 (b). Considering the constraints of the Ricean factor and energy-related parameters for different propagation scenarios as mentioned in Section II, we choose the following parameters in order to fit the measured Doppler PSDs reported in [6] for the two scenarios with low VTD: 1)  $K = 2.186$ ,  $\eta_{DB} = 0.005$ ,  $\eta_{SB_1} = 0.252$ ,  $\eta_{SB_2} = 0.262$ , and  $\eta_{SB_3} = 0.481$  for Fig. 7 (a); 2)  $K = 3.786$ ,  $\eta_{DB} = 0.051$ ,  $\eta_{SB_1} = 0.335$ ,  $\eta_{SB_2} = 0.203$ , and  $\eta_{SB_3} = 0.411$  for Fig. 7 (b). The excellent agreement between the theoretical results and measured data confirms the utility of the proposed model. The environment-related parameters for high VTD in Figs. 7 (a) and (b) are the same as those for low VTD except  $k_T^{TR} = k_R^{TR} = 0.6$ , which are related to the distribution of moving cars (normally, the smaller values the more distributed moving cars, i.e., the higher VTD). The Doppler PSDs for high VTD shown in Figs. 7 (a) and (b) were obtained with the parameters  $K=0.2$ ,  $\eta_{DB} = 0.715$ ,  $\eta_{SB_1} = \eta_{SB_2} = 0.115$ , and  $\eta_{SB_3} = 0.055$ . Unfortunately, to the best of the authors' knowledge, no measurement results (e.g., in [4]–[9]) were available regarding the impact of high VTD (e.g., a traffic jam) on the Doppler PSD.

Comparing the theoretical Doppler PSDs in Figs. 7 (a) and (b), we observe that the VTD significantly affects both the shape and value of the Doppler PSD for M2M channels. The Doppler PSD tends to be more evenly distributed across all Doppler frequencies with a higher VTD. This is because with a high VTD, the received power mainly comes from the moving cars around the Tx and Rx from all directions, while

the power of the line-of-sight (LoS) component is not that significant. This means that the received power for different Doppler frequencies (directions) is more evenly distributed. With a low VTD, the received power from the LoS component may be significant, while the power from the moving cars may be small. Therefore, the power tends to be concentrated on some Doppler frequencies.

## V. CONCLUSION

In this paper, we have proposed a generic and adaptive GBSM for non-isotropic MIMO M2M Ricean fading channels. By adjusting some model parameters and with the help of the newly derived general relationship between the AoA and AoD, the proposed model is adaptable to a wide variety of M2M propagation environments. In addition, the VTD is for the first time taken into account in the GBSM for modeling M2M channels. From this model, we have derived the STF CF and the corresponding SDF PSD for non-isotropic scattering environments, where the closed-form expressions are available in the case of the single-bounce two-ring model for macro-cell and micro-cell scenarios, and the double-bounce two-ring model for any scenarios. Based on the derived STF CFs and SDF PSDs, we have further investigated the degenerate CFs and PSDs in detail and found that some parameters (e.g., the angle spread, direction of motion, antenna element spacing, etc.) and the VTD have a great impact on the resulting CFs and PSDs. It has also been demonstrated that for M2M isotropic scenarios, no matter what the direction of motion and shape of the scattering region are, single-bounced rays will result in the U-shaped Doppler PSD, while double-bounced rays will result in the “rounded”-shaped Doppler PSD. Finally, it has been shown that theoretical Doppler PSDs match the measured data in [6], validating the utility of our model.

## APPENDIX

### A. DERIVATIONS OF (13)–(18)

In this appendix, following the same derivation procedure (i.e., the same newly proposed method), we will derive these general relationships for the two-ring model in (13)–(16) and the ellipse model in (17) and (18). In Fig. 1, applying the laws of cosines and sines to the triangle  $O_T s^{(n_1)} O_R$ , we obtain  $\xi_{n_1}^2 = R_T^2 + D^2 - 2DR_T \cos \phi_T^{(n_1)}$ ,  $R_T^2 = \xi_{n_1}^2 + D^2 + 2D\xi_{n_1} \cos \phi_T^{(n_1)}$ , and  $R_T / \sin \phi_T^{(n_1)} = \xi_{n_1} / \sin \phi_T^{(n_1)}$ . From the above expressions, we can easily obtain (13) and (14). Similarly, applying the laws of cosines and sines to the triangle  $O_T s^{(n_2)} O_R$ , we have  $\xi_{n_2}^2 = R_R^2 + D^2 + 2DR_R \cos \phi_T^{(n_2)}$ ,  $R_R^2 = \xi_{n_2}^2 + D^2 - 2D\xi_{n_2} \cos \phi_T^{(n_2)}$ , and  $R_R / \sin \phi_T^{(n_2)} = \xi_{n_2} / \sin \phi_T^{(n_2)}$ . We can easily obtain (15) and (16) from these expressions. Analogously, applying the laws of cosines and sines to the triangle  $O_T s^{(n_3)} O_R$ , we get  $(\xi_T^{(n_3)})^2 = (\xi_R^{(n_3)})^2 + D^2 + 2D\xi_R^{(n_3)} \cos \phi_R^{(n_3)}$ ,  $(\xi_R^{(n_3)})^2 = (\xi_T^{(n_3)})^2 + D^2 - 2D\xi_T^{(n_3)} \cos \phi_T^{(n_3)}$ , and  $\xi_R^{(n_3)} / \sin \phi_T^{(n_3)} = \xi_T^{(n_3)} / \sin \phi_R^{(n_3)}$ . Based on the above expressions, and the following equalities  $D=2f$  and  $\xi_T^{(n_3)} + \xi_R^{(n_3)} = 2a$ , we can get (17) and (18).

## B. DERIVATION OF (23)

Considering the von Mises PDF for the two-ring model, applying the following approximate relationships  $\phi_R^{(n_1)} \approx \pi - \Delta_T \sin \phi_T^{(n_1)}$  and  $\phi_T^{(n_2)} \approx \Delta_R \sin \phi_R^{(n_2)}$ , and substituting (3) and (6)–(9) into (19), we have

$$\rho_{h_{pq}^{SB_1(2)} h_{p'q'}^{SB_1(2)}}(\tau, \chi) = \frac{\left[ 2\pi I_0 \left( k_{T(R)}^{SB_1(2)} \right) \right]^{-1} e^{jC_{T(R)}^{SB_1(2)}}}{\sqrt{(K_{pq}+1)(K_{p'q'}+1)}} \times \int_{-\pi}^{\pi} e^{\left( A_{T(R)}^{SB_1(2)} \cos \phi_{T(R)}^{SB_1(2)} + B_{T(R)}^{SB_1(2)} \sin \phi_{T(R)}^{SB_1(2)} \right)} d\phi_{T(R)}^{SB_1(2)} \quad (35)$$

where  $A_{T(R)}^{SB_1(2)}$ ,  $B_{T(R)}^{SB_1(2)}$ , and  $C_{T(R)}^{SB_1(2)}$  have been given in (24a)–(24f). The definite integrals in the right hand side of (35) can be solved by using the equality  $\int_{-\pi}^{\pi} e^{a \sin c + b \cos c} dc = 2\pi I_0(\sqrt{a^2 + b^2})$  [25]. After some manipulation, we can get the closed-form expression (23).

## C. DERIVATION OF (30)

Given  $a^2 + b^2 = c(d^2 + e^2)$ , after some complex manipulation, we can rewrite  $I_0 \left[ \sqrt{\left( A_{T(R)}^{SB_1(2)} \right)^2 + \left( B_{T(R)}^{SB_1(2)} \right)^2} \right]$  as

$$I_0 \left[ j \sqrt{W_{T(R)}^{SB_1(2)}} \sqrt{\left( \tau + \frac{D_{T(R)}^{SB_1(2)}}{W_{T(R)}^{SB_1(2)}} \right)^2 + \left( \frac{E_{T(R)}^{SB_1(2)}}{W_{T(R)}^{SB_1(2)}} \right)^2} \right] \quad (36)$$

where  $W_{T(R)}^{SB_1(2)}$ ,  $D_{T(R)}^{SB_1(2)}$ , and  $E_{T(R)}^{SB_1(2)}$  have been given in (31b)–(31d). Note that the expression (36) corrects the expressions (38) and (39) in [14]. By applying the Fourier transform to (23) in terms of the time separation  $\tau$  and using (36) and the equality  $\int_0^{\infty} I_0 \left( j\alpha \sqrt{x^2 + y^2} \right) \cos(\beta x) dx = \cos \left( y \sqrt{\alpha^2 - \beta^2} \right) / \sqrt{\alpha^2 - \beta^2}$  [25], we can obtain (30).

## D. COMPARISON BETWEEN THE DOPPLER PSDS WITH DIFFERENT CFS (19) AND (20)

To further clarify which CF definition, (19) or (20), results in the correct Doppler PSD to accurately reflect the underlying physical phenomena of real channels, we first derive the relationship between the Doppler PSD based on the CF (19),  $S_{h_{pq}h_{pq}}(f_D)$ , and the Doppler PSD based on the CF (20),  $\tilde{S}_{h_{pq}h_{pq}}(f_D)$ . Considering the equality  $\tilde{\rho}_{h_{pq}h_{pq}}(\tau) = \rho_{h_{pq}h_{pq}}^*(\tau)$  and the Fourier transform relation between the CF and Doppler PSD, we have

$$\tilde{S}_{h_{pq}h_{pq}}(f_D) = S_{h_{pq}h_{pq}}^*(-f_D). \quad (37)$$

From (37), it is clear that only if  $S_{h_{pq}h_{pq}}(f_D)$  is a real function and symmetrical to the origin, the equality  $\tilde{S}_{h_{pq}h_{pq}}(f_D) = S_{h_{pq}h_{pq}}(f_D)$  holds. Note that due to the Fourier transform relationship, the equality  $\tilde{S}_{h_{pq}h_{pq}}(f_D) = S_{h_{pq}h_{pq}}(f_D)$  leads to the equality  $\tilde{\rho}_{h_{pq}h_{pq}}(\tau) = \rho_{h_{pq}h_{pq}}(\tau)$  and vice versa. We now proceed the comparison of  $S_{h_{pq}h_{pq}}(f_D)$  and  $\tilde{S}_{h_{pq}h_{pq}}(f_D)$  in the following two typical scenarios.

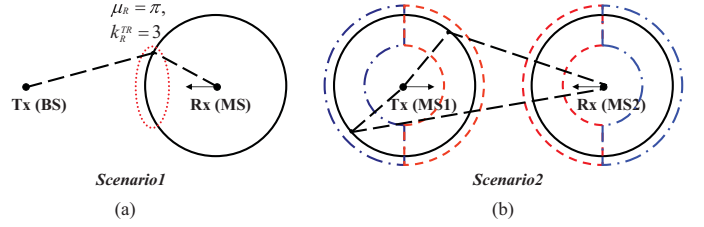


Fig. 8. Graphical description of (a) *Scenario1* and (b) *Scenario2*.

The first typical scenario, *Scenario1*, is a non-isotropic F2M macro-cell propagation environment ( $f_{T_{max}} = 0$ ), as shown in Fig. 8(a). We use a one-ring model to represent this scenario, where the ring of scatterers is around the Rx, i.e., mobile station (MS), and the MS moves toward the direction of the Tx, i.e.,  $\gamma_R = \pi$ . Note that the major amount of scatterers are located in a small part of the ring facing the motion of the MS, i.e.,  $\mu_R = \pi$ . The second scenario, *Scenario2*, is an isotropic M2M propagation environment ( $k_T^{TR} = k_R^{TR} = 0$ ), where the Tx and Rx move in opposite directions ( $\gamma_T = 0$  and  $\gamma_R = \pi$ ), as shown in Fig. 8(b). Here, a single-bounce two-ring model is used to represent this scenario. For *Scenario1*, based on (37), the opposite results for the Doppler PSD are expected as shown in Fig. 9, where  $k_R^{TR} = 3$ . Since the MS moves toward the majority of received signals, the maximum Doppler PSD should appear at  $f_D = f_{R_{max}} = 570$  Hz. From Fig. 9, it is clear that the  $S_{h_{pq}h_{pq}}(f_D)$  presents the underlying physical phenomena for *Scenario1*. For *Scenario2*, as expected from (37), the opposite results of the Doppler PSD with respect to the range of Doppler frequencies are illustrated in Fig. 9, where  $f_{T_{max}} = f_{R_{max}} = 570$  Hz were used. Since the Tx and Rx are moving in opposite directions, the Doppler PSD should be limited to the range of Doppler frequencies  $0 \leq f_D \leq 1140$  Hz, whereas the maximum Doppler PSD exists at  $f_D = 0$  and  $f_D = f_{T_{max}} + f_{R_{max}} = 1140$  Hz. Again, from Fig. 9, it is obvious that  $S_{h_{pq}h_{pq}}(f_D)$  reflects the underlying physical phenomenon for *Scenario2*. Therefore, we can conclude that  $S_{h_{pq}h_{pq}}(f_D)$  is able to accurately capture the underlying physical phenomena of real channels for any scenarios, while  $\tilde{S}_{h_{pq}h_{pq}}(f_D)$  cannot. It is worth stressing that for an isotropic F2M macro-cell scenario (Clarke's scenario), where no scatterers are around the Tx, we find that the difference of the Doppler PSD caused by two CF definitions vanishes, i.e.,  $\tilde{S}_{h_{pq}h_{pq}}(f_D) = S_{h_{pq}h_{pq}}(f_D)$ . This is because Clarke's scenario has the U-shape Doppler PSD, which is a real function and symmetrical to the origin. This seems to be the reason why the CF (20) was widely misapplied.

## REFERENCES

- [1] R. Wang and D. Cox, "Channel modeling for ad hoc mobile wireless networks," in *Proc. IEEE VTC'02-Spring*, Birmingham, USA, May 2002, pp. 21–25.
- [2] F. Kojima, H. Harada, and M. Fujise, "Inter-vehicle communication network with an autonomous relay access scheme," *IEICE Trans. Commun.*, vol. E83-B, no. 3, pp. 566–575, Mar. 2001.
- [3] IEEE P802.11p/D2.01, "Standard for wireless local area networks providing wireless communications while in vehicular environment," Tech. Rep., Mar. 2007.
- [4] J. Maurer, T. Fügen, and W. Wisebeck, "Narrow-band measurement and analysis of the inter-vehicle transmission channel at 5.2 GHz," in *Proc. IEEE VTC'02-Spring*, Birmingham, USA, May 2002, pp. 1274–1278.

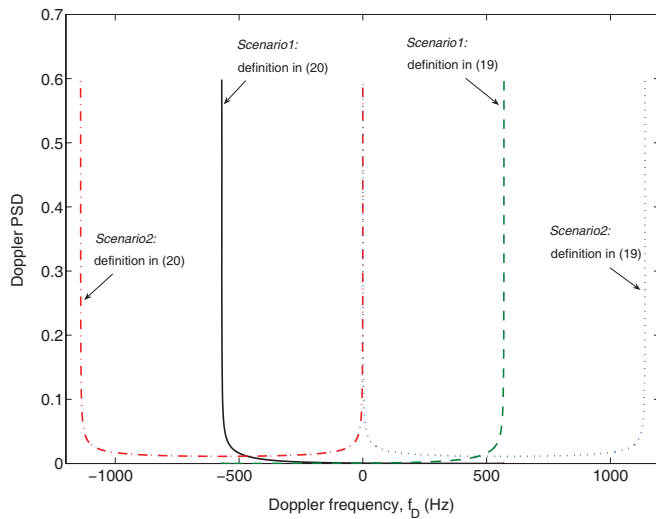


Fig. 9. Comparison of the Doppler PSDs of *Scenario1* and *Scenario2* based on the CF definitions in (19) and (20).

- [5] G. Acosta, K. Tokuda, and M. A. Ingram, "Measured joint Doppler-delay power profiles for vehicle-to-vehicle communications at 2.4 GHz," in *Proc. IEEE GLOBECOM'04*, Dallas, USA, Nov. 2004, pp. 3813–3817.
- [6] G. Acosta and M. A. Ingram, "Six time- and frequency-selective empirical channel models for vehicular wireless LANs," *IEEE Veh. Technol. Mag.*, vol. 2, no. 4, pp. 4–11, Dec. 2007.
- [7] L. Cheng, B. E. Henty, D. D. Stancil, F. Bai, and P. Mudalige, "Mobile vehicle-to-vehicle narrowband channel measurement and characterization of the 5.9 GHz dedicated short range communication (DSRC) frequency band," *IEEE J. Select. Areas Commun.*, vol. 25, no. 8, pp. 1501–1516, Oct. 2007.
- [8] I. Sen and D. W. Matolak, "Vehicle-vehicle channel models for the 5-GHz band," *IEEE Trans. Intell. Transp. Syst.*, vol. 9, no. 2, pp. 235–245, June 2008.
- [9] A. Paier, J. Karedal, N. Czink, C. Dumard, T. Zemen, F. Tufvesson, A. F. Molisch, and C. F. Mecklenbräuker, "Characterization of vehicle-to-vehicle radio channels from measurements at 5.2 GHz," *Wireless Pers. Commun.*, June 2008. [Online] <http://dx.doi.org/10.1007/s11277-008-9546-6>.
- [10] J. Maurer, T. Fügen, M. Porebska, T. Zwick, and W. Wisebeck, "A ray-optical channel model for mobile to mobile communications," *COST 2100 4th MCM*, COST 2100 TD(08) 430, Wroclaw, Poland, Feb. 2008.
- [11] A. S. Akki and F. Haber, "A statistical model for mobile-to-mobile land communication channel," *IEEE Trans. Veh. Technol.*, vol. 35, no. 1, pp. 2–10, Feb. 1986.
- [12] A. S. Akki, "Statistical properties of mobile-to-mobile land communication channels," *IEEE Trans. Veh. Technol.*, vol. 43, no. 4, pp. 826–831, Nov. 1994.
- [13] M. Pätzold, B. O. Hogstad, and N. Youssef, "Modeling, analysis, and simulation of MIMO mobile-to-mobile fading channels," *IEEE Trans. Wireless Commun.*, vol. 7, no. 2, pp. 510–520, Feb. 2008.
- [14] A. G. Zajić and G. L. Stüber, "Space-time correlated mobile-to-mobile channels: modeling and simulation," *IEEE Trans. Veh. Technol.*, vol. 57, no. 2, pp. 715–726, Mar. 2008.
- [15] A. F. Molisch, "A generic model for MIMO wireless propagation channels in macro- and microcells," *IEEE Trans. Signal Process.*, vol. 51, no. 1, pp. 61–71, Jan. 2004.
- [16] C.-X. Wang, M. Pätzold, and Q. Yao, "Stochastic modeling and simulation of frequency correlated wideband fading channels," *IEEE Trans. Veh. Technol.*, vol. 56, no. 3, pp. 1050–1063, May 2007.
- [17] A. Abdi and M. Kaveh, "A space-time correlation model for multielement antenna systems in mobile fading channels," *IEEE J. Select. Areas Commun.*, vol. 20, no. 3, pp. 550–560, Apr. 2002.
- [18] X. Cheng, C.-X. Wang, and D. I. Laurenson, "A generic space-time-frequency correlation model and its corresponding simulation model for MIMO wireless channels," in *Proc. EuCAP'07*, Edinburgh, UK, Nov. 2007, pp. 1–6.
- [19] A. Papoulis and S. U. Pillai, *Probability, Random Variables and Stochastic Processes*, 4th ed. New York: McGraw Hill, 2002.
- [20] M. Pätzold and N. Youssef, "Modeling and simulation of direction-selective and frequency-selective mobile radio channels," *International J. Electron. and Commun.*, vol. 55, no. 6, pp. 433–442, Nov. 2001.
- [21] P. Y. Chen and H. J. Li, "Modeling and applications of space-time correlation for MIMO fading signals," *IEEE Trans. Veh. Technol.*, vol. 56, no. 4, pp. 1580–1590, July 2007.
- [22] G. L. Stüber, *Principles of Mobile Communication*, 2nd ed. Boston: Kluwer Academic Publishers, 2001.
- [23] A. Abdi, J. A. Barger, and M. Kaveh, "A parametric model for the distribution of the angle of arrival and the associated correlation function and power spectrum at the mobile station," *IEEE Trans. Veh. Technol.*, vol. 51, no. 3, pp. 425–434, May 2002.
- [24] S. Wang, A. Abdi, J. Salo, H. M. EL-Sallabi, J. W. Wallace, P. Vainikainen, and M. A. Jensen, "Time-varying MIMO channels: parametric statistical modeling and experimental results," *IEEE Trans. Veh. Technol.*, vol. 56, no. 4, pp. 1949–1963, July 2007.
- [25] I. S. Gradshteyn and I. M. Ryzhik, *Table of Integrals, Series, and Products*, 6th ed. Boston: Academic, 2000.



**Xiang Cheng** (S'05) received the BSc and MEng degrees in communication and information systems from Shandong University, China, in 2003 and 2006, respectively. Since October 2006, he has been a PhD student at Heriot-Watt University, Edinburgh, UK. His current research interests include mobile propagation channel modeling and simulation, multiple antenna technologies, mobile-to-mobile communications, and cooperative communications. He has published more than 20 research papers in journals and conference proceedings. Mr. Cheng was

awarded the Postgraduate Research Prize from Heriot-Watt University in 2007 and 2008, respectively, for academic excellence and outstanding performance. He served as a TPC member for IEEE HPCC2008 and IEEE CMC2009.



**Cheng-Xiang Wang** (S'01-M'05-SM'08) received the BSc and MEng degrees in communication and information systems from Shandong University, China, in 1997 and 2000, respectively, and the PhD degree in wireless communications from Aalborg University, Denmark, in 2004.

Dr Wang has been a lecturer at Heriot-Watt University, Edinburgh, UK since 2005. He is also an honorary fellow of the University of Edinburgh, UK, a guest researcher of Xidian University, China, and an adjunct professor of Guilin University of Electronic Technology, China. He was a research fellow at the University of Agder, Norway, from 2001–2005, a visiting researcher at Siemens AG-Mobile Phones, Munich, Germany, in 2004, and a research assistant at Technical University of Hamburg-Harburg, Germany, from 2000–2001. His current research interests include wireless channel modelling and simulation, cognitive radio networks, mobile-to-mobile communications, cooperative communications, cross-layer design, MIMO, OFDM, UWB, wireless sensor networks, and (beyond) 4G. He has published 1 book chapter and over 110 papers in journals and conferences.

Dr Wang serves as an editor for IEEE TRANSACTIONS ON WIRELESS COMMUNICATIONS, WILEY WIRELESS COMMUNICATIONS AND MOBILE COMPUTING JOURNAL, WILEY SECURITY AND COMMUNICATION NETWORKS JOURNAL, and JOURNAL OF COMPUTER SYSTEMS, NETWORKS, AND COMMUNICATIONS. He served or is serving as a TPC chair for CMC 2009, publicity chair for CrownCom 2009, TPC symposium co-chair for IWCMC 2009, General Chair for VehiCom 2009, and TPC vice-chair or member for more than 35 international conferences. Dr Wang is listed in *Dictionary of International Biography 2008 and 2009*, *Who's Who in the World 2008 and 2009*, *Great Minds of the 21st Century 2009*, and *2009 Man of the Year*.



**David I. Laurenson** (M'90) is currently a Senior Lecturer at The University of Edinburgh, Scotland. His interests lie in mobile communications: at the link layer this includes measurements, analysis and modelling of channels, whilst at the network layer this includes provision of mobility management and Quality of Service support. His research extends to practical implementation of wireless networks to other research fields, such as prediction of fire spread using wireless sensor networks (<http://www.firegrid.org>), to deployment of communication networks for distributed control of power distribution networks. He is an associate editor for Hindawi journals, and acts as a TPC member for international communications conferences. He is a member of the IEEE and the IET.



**Sana Salous** (M'95) received the B.E.E. degree from the American University of Beirut, Beirut, Lebanon, in 1978 and the M.Sc. and Ph.D. degrees from the University of Birmingham, Birmingham, U.K., in 1979 and 1984, respectively. She was an Assistant Professor with Yarmouk University, Irbid, Jordan, until 1988 and a Research Associate with the University of Liverpool, Liverpool, U.K., until 1989, at which point, she took up a lecturer post with the Department of Electronic and Electrical Engineering, University of Manchester Institute of

Science and Technology (UMIST), Manchester, U.K. In 2003 she took up the Chair in Communications Engineering with the School of Engineering, Durham University, Durham, U.K, where she is currently the Director of the Centre for Communications Systems.



**Athanasios V. Vasilakos** (M'89) is currently Professor at the Dept. of Computer and Telecommunications Engineering, University of Western Macedonia, Greece, and Visiting Professor at the Graduate Programme of the Dept. of Electrical and Computer Engineering, National Technical University of Athens (NTUA). He is coauthor (with W. Pedrycz) of the books *Computational Intelligence in Telecommunications Networks* (CRC press, USA, 2001), *Ambient Intelligence, Wireless Networking, Ubiquitous Computing* (Artech House, USA, 2006),

coauthor (with M. Parashar, S. Karnouskos, W. Pedrycz) *Autonomic Communications* (Springer, to appear), *Arts and Technologies* (MIT Press, to appear), coauthor (with Yan Zhang, Thrasyvoulos Spyropoulos) *Delay Tolerant Networking* (CRC press, to appear), coauthor (with M. Anastasopoulos) *Game Theory in Communication Systems* (IGI Inc, USA, to appear). He has published more than 200 articles in top international journals (i.e. IEEE/ACM TRANSACTIONS ON NETWORKING, IEEE TRANSACTIONS ON INFORMATION THEORY, IEEE JOURNAL ON SELECTED AREAS IN COMMUNICATIONS, IEEE TRANSACTIONS ON WIRELESS COMMUNICATIONS, IEEE TRANSACTIONS ON NEURAL NETWORKS, IEEE TRANSACTIONS ON SYSTEMS, MAN, AND CYBERNETICS, IEEE T-ITB, IEEE T-CIAIG, etc) and conferences. He is the Editor-in-chief of the Inderscience Publishers journals: *INTERNATIONAL JOURNAL OF ADAPTIVE AND AUTONOMOUS COMMUNICATIONS SYSTEMS (IJAACS)*, *INTERNATIONAL JOURNAL OF ARTS AND TECHNOLOGY*. He was or is at the editorial board of more than 20 international journals including: *IEEE COMMUNICATIONS MAGAZINE* (1999-2002 and 2008-), *IEEE TRANSACTIONS ON SYSTEMS, MAN AND CYBERNETICS (TSMC, Part B, 2007-)*, *IEEE TRANSACTIONS ON WIRELESS COMMUNICATIONS* (invited), *IEEE TRANSACTIONS ON INFORMATION THEORY IN BIOMEDICINE (TITB, 2009-)*, etc. He chairs several conferences, e.g., *ACM IWCMC'09*, *ICST/ACM Autonomics 2009*. He is a chairman of the Telecommunications Task Force of the Intelligent Systems Applications Technical Committee (ISATC) of the IEEE Computational Intelligence Society (CIS). Senior Deputy Secretary-General and fellow member of ISIBM [www.isibm.org](http://www.isibm.org) (International Society of Intelligent Biological Medicine (ISIBM)). He is member of the IEEE and ACM.